Contents lists available at ScienceDirect

Thin Solid Films

journal homepage: www.elsevier.com/locate/tsf

Dielectric response and structure of amorphous hydrogenated carbon films with nitrogen admixture

Lenka Zajíčková [a,*], Daniel Franta [a], David Nečas [a], Vilma Buršíková [a], Mihai Muresan [a], Vratislav Peřina [b], Christoph Cobet [c]

[a] Department of Physical Electronics, Faculty of Science, Masaryk University, Kotlářská 2, 611 37 Brno, Czech Republic
[b] Institute of Nuclear Physics, Academy of Science of the Czech Republic, Řež, Czech Republic
[c] Institute for Analytical Sciences, Albert-Einstein-Str. 9, 12489 Berlin, Germany

ARTICLE INFO

ABSTRACT

The optical properties and structure of a-C:H films were modified by addition of nitrogen into the CH_4/H_2 deposition mixture. Three films prepared in capacitively coupled rf discharge were compared: (a) hydrogenated diamond like carbon film with hydrogen content of 34% and indentation hardness of 21.7 GPa, (b) hard a-C:H:N film with nitrogen content of 13% and indentation hardness of 18.5 GPa and (c) soft a-C:H:N film with nitrogen content of 10% and indentation hardness of 6.7 GPa. It is shown how the parametrized density of states model describing dielectric response of electronic interband transitions can be applied to modified a-C:H:N and how it can be combined with correct treatment of transmittance measured in infrared range using additional Gaussian peaks in joint density of phonon states. This analysis resulted in determination of film dielectric function in wide spectral range (0.045–30 eV) and provided also information about the density of states of valence and conduction bands and lattice vibrations.

1. Introduction

There are many forms of amorphous carbon with great variety of physical properties depending on the specific mixture of sp^3 and sp^2 sites. If they contain hydrogen its content additionally influences the material structure and properties. An a-C or a-C:H of higher sp^3 content belongs to the class of materials often called diamond-like carbon (DLC). Casiraghi suggested more precise classification of a-C:H films into four types [1,2]: (a) polymer-like a-C:H (PLCH) with the highest H content (40–60 at.%), up to 70% sp^3 but soft and of low density, (b) harder diamond-like a-C:H (DLCH) with intermediate H content (20–40 at.%), (c) hydrogenated tetrahedral amorphous carbon films (ta-C:H) in which the C–C sp^3 content is increased (as compared to DLCH) whilst keeping a fixed H content 25–30 at.% H and (d) graphite-like a-C:H (GLCH) with less than 20 at.% of H, a high sp^2 content and sp^2 clustering.

PLCH films are soft, have low density and the optical gap ranges from 2 to 4 eV. Even if DLCH films have lower overall sp^3 content, they have more C–C sp^3 bonds than PLCH. Thus, they have better mechanical properties. Their optical gap is between 1 and 2 eV. Films defined as ta-C:H differ from DLCHs by their Raman spectra, higher density (up to

2.4 g/cm^3) and Young's modulus (up to 300 GPa) [3–5]. Their optical gap can reach 2.4 eV [6]. The gap of GLCH is under 1 eV.

The optical gap in the above material classification was determined from the decrease of absorption coefficient to 10^4 cm^{-1}, so called E_{04}, or from Tauc plot. This approach provides information about the film transparency but does not describe the nature of sp^3/sp^2 carbon materials because two different types of states in valence and conduction bands form the density of states (DOS), the states related to σ and π electrons. Therefore, two different band gaps, corresponding to $\sigma \rightarrow \sigma^*$ and $\pi \rightarrow \pi^*$ interband transitions, should be distinguished. In this aspect a-C(:H) material differ from amorphous semiconductors such as a-Si [7] and classification using the optical gap can be confusing.

The a-C(:H) coatings have wide range of applications but it is necessary to optimize their adhesion to substrate material and decrease intrinsic stress in the films. Approaches solving this problem include the fabrication of an intermediate layer between the coating and substrate, and the reduction of the internal stress of the coating. Intermediate metal or compound layers such as Ti, Zr, W, Nb, or WC have shown potential to improve the adhesive strength [8]. The great disadvantage of this technique is that two or more steps, sometimes using different deposition techniques, are necessary. A prospective trend is to use a single step process by mixing some dopants into the structure of DLC. The residual stress of the DLC coating has been reduced by including additional elements. Positive results were achieved by Rabbani [9] for nitrogen admixture.

* Corresponding author. Tel.: +420 54949 8217; fax: +420 541211214.
E-mail address: lenkaz@physics.muni.cz (L. Zajíčková).

The optical properties and structure of a-C:H are modified by nitrogen addition. Hayashi [10] observed a decrease of the optical gap with the increase of nitrogen content. Nitrogen addition decreased refractive index due to lower density of the material [11]. Recently, we have shown for DLCH films that optical measurement performed from near infrared to extreme ultraviolet (NIR-XUV) range can be analyzed using parametrization of DOS (PDOS) and, therefore, provide information about valence and conduction bands [12,13]. This work aims to show how the PDOS model can be applied to a-C:H:N and how it can be combined with correct treatment of transmittance measured in infrared range using additional Gaussian peaks in joint density of states (JDOS). This approach results not only in the knowledge of film dielectric function in wide spectral range but provides also information about DOS of valence and conduction bands and lattice vibrations.

2. Experimental details

Thin films were deposited in radio frequency (rf) capacitively coupled discharge driven at the frequency of 13.56 MHz. A detailed drawing of the plasma reactor can be found in Ref. [14]. Pumping system consisted of turbo and rotary pumps. The reactor chamber was made of stainless steel and equipped with two parallel plate electrodes. The upper showerhead electrode, 380 mm in diameter, was grounded and used for gas distribution. The bottom electrode, 420 mm in diameter, was connected to an rf generator through a matching network. The distance between the electrodes was 55 mm.

This paper discusses two a-C:H:N films prepared from the mixture of $CH_4/H_2/N_2$, labeled CH16 and CH17, and one DLCH film (CH30) prepared from CH_4/H_2 mixture for comparison. The flow rate of CH_4 was 8.5 sccm. The flow rate of H_2 was 5 sccm in case of CH30 whereas 2.5 sccm of H_2 and 2.5 sccm of N_2 were used for CH17 and CH16. The total pressure was 12 Pa.

The substrates, double-side polished crystalline silicon (Si) pieces, were placed on the rf electrode. This electrode was dc self-biased due to a reactor asymmetry, i.e. smaller area of rf electrode as compared to grounded surfaces, and different mobility of electrons and ions [15]. The bias U_b determined the energy of ions bombarding a growing film. RF power and bias used for deposition of studied films are summarized in Table 1.

The Si substrates were treated in H_2/Ar plasma before the deposition. The flow rate of H_2 and Ar were 10 and 3 sccm, respectively. The total pressure was 8 Pa. The discharge was operated at 100 W and corresponding dc self-bias was − 150V. The treatment time was 10 min.

The thin films on Si substrates were optically characterized as follows:

- Ellipsometry in NIR-UV range (0.6–6.5 eV) measured with Jobin Yvon UVISEL phase-modulated (PM) variable-angle spectroscopic ellipsometer at five angles of incidence from 55° to 75°.

- Ellipsometry in UV–VUV range (5–9.6 eV) measured with BESSY II synchrotron rotating-analyzer (RA) ellipsometer without retarder at fixed angle of incidence. The angle of incidence was 67.5° and the set of two MgF_2-Rochon prisms were used as polarizer and analyzer.
- Ellipsometry in XUV range (9–30 eV) measured with BESSY II synchrotron ellipsometer with triple reflection polarizers at 45° angle of incidence. This measurement was carried out only for DLCH film CH30 [13].
- Reflectance in NIR-UV range (1.24–6.5 eV) measured with PerkinElmer Lambda 45 spectrophotometer with reflectance accessory at 6°.
- Transmittance in IR range (0.045–0.93 eV, i.e. 370–7500 cm^{-1}) measured with Bruker Vertex 80v Fourier transform spectrophotometer equipped with a parallel beam transmittance accessory for correct absolute transmittance measurement.

The hardness and elastic modulus values were assessed from depth sensing indentation tests using the Fischerscope H100 tester with Berkovich indenter. The load and the corresponding indentation depth were recorded as a function of time for both loading and unloading processes. The desired material parameters were obtained from analysis of loading and unloading curves. The indentation tests were carried out for several different indentation depths (i.e. several different applied loads) in order to map the mechanical properties of the film/substrate system from near surface up to the film-substrate interface. The applied load L ranged from 1 to 100 mN with the force resolution of 0.04 mN. The accuracy of the indentation depth measurement was ± 1 nm. Each indentation test was repeated at least 16 times.

The atomic composition was determined by Rutherford backscattering (RBS) and elastic recoil detection (ERDA) methods using a INP Van de Graaf generator and TANDETRON with a linear electrostatic accelerators. The contents of C, N and O were measured by RBS using 1.74 MeV and 2.3 MeV protons and 3.04 MeV α-particles as projectiles. Higher Rutherford cross-section values enhanced the backscattering spectrometry sensitivity as follows: at 2.3 MeV protons for C approximately sevenfold, for N sixfold, for O fourfold, at 1.74 MeV protons for C by approximately 70× and at 3.04 MeV α-particles for O by 23×. A surface barrier detector was used for the detection of particles scattered under the laboratory scattering angle of 170°. The particles impinging at 60° to the surface normal were used for enhancement of measurement sensitivity because studied films were quite thin. Anyway, the accuracy of evaluation was not high especial as concerns film density. The depth resolution was from some tens of nanometers due to the finite energy resolution of the detector.

The ERDA with an incident beam of 2.75 MeV α-particles at 75° to the surface normal was used for the measurement of H content. Hydrogen atoms recoiled at 30° were detected with a surface barrier detector covered with a 12 μm thick mylar stopping foil. The foil filtered out reflected α-particles and protected the detector. The charge of impinging α-particles was measured using beam chopper with Au layer and monitored in RBS configuration. For proper evaluation the "dead time" is considered. The ERDA was calibrated using 11.9% H:Si standard. The RBS and ERDA measurements were evaluated by computer codes GISA 3 [16] and SIMNRA [17], respectively, using cross-section values from a SigmaBase [18].

3. Results and discussion

Data measured with all optical instruments were fitted simultaneously using a single, consistent structural and dispersion model. The samples were modeled by the system consisting of Si substrate, whose optical constants were determined with high precision in previous experiments, an inhomogeneous transition layer and an inhomogeneous anisotropic film. The transition layer originated from interaction of plasma with Si substrate whose surface region is modified during a plasma pretreatment and the initial phase of the

Table 1
Summary of varying deposition parameters, i.e. power P and dc self-bias U_b, film thickness d, elemental composition and mechanical properties (indentation hardness H_{IT} and indentation modulus E_{IT}) of studied films.

Parameter/film	CH30	CH16	CH17
P (W)	100	100	50
U_b (V)	− 80	− 130	− 50
d (nm)	101	114	216
C (%)	65	56	46
H (%)	34	28	38
N (%)	0	13	10
O (%)	1	3	6
H_{IT} (GPa)	21.7	18.5	6.7
E_{IT} (GPa)	155	130	68

deposition. Dispersion models used for fitting were Kramers–Kronig consistent. Optical measurements in NIR–XUV provided information about electronic band structure of deposited films and transition layers whereas phonon response in IR range revealed the presence of chemical groups in studied materials.

3.1. Analysis of interband transitions

Electronic dielectric responses of a-C:H(:N) films were constructed using parametrization of density of states (PDOS) [12,19]. Schematic diagram of the density of states (DOS) of a-C:H:N material is in Fig. 1. It is similar to DOS of pure a-C:H, aside from the addition of nitrogen 1s core level states, because 2s and 2p valence electrons of carbon and nitrogen atoms form common valence and conduction bands of a-C:H:N material. Since nitrogen and carbon can form multiple bonds two groups of electron states, π and σ, have to be considered. The valence bands correspond to the π and σ bonding states while the conduction bands to the π and σ antibonding states. The presence of hydrogen in the material increases the density of σ states but π states are not influenced because hydrogen valence 1s electrons form only single bonds. Excited levels, i.e. 2s, 2p etc. of H and 3s, 3p etc. of C and N, form higher excitation bands ξ of the material.

Excitations of carbon and nitrogen core electrons contribute to the dielectric response from energies 285 and 400 eV, respectively. Therefore, only transitions from valence, π and σ, to conduction, π and σ, or higher excitation, ξ, bands contribute to the dielectric response in NIR–XUV range. The contribution of electronic transitions to the imaginary part of the dielectric function ε_i was, in our model, calculated as a sum of three terms [20]

$$\varepsilon_i(E) = \varepsilon_{i,\pi\rightarrow\pi*}(E) + \varepsilon_{i,\sigma\rightarrow\sigma*}(E) + \varepsilon_{i,\sigma\rightarrow\xi*}(E) \qquad (1)$$

where E is photon energy. The individual contributions can be expressed as

$$\varepsilon_{i,j\rightarrow k*}(E) = \frac{1}{E^2}\int_{-\infty}^{\infty} N_j(S)N_{k*}(S+E)dS, \qquad (2)$$

where $j,k = \pi,\sigma,\xi$. Density of states N_j and N_k* were parametrized by six parameters for π and σ bands and three parameters for higher excitation states $\xi*$, i.e. the $6+6+3$ PDOS model [12] was used. Dispersion model parameters found for all three films (one DLCH and two a-C:H:N) are summarized in Table 2. Their physical meaning is following: Q_j is proportional to the product of electron density and corresponding transition probability; E_{gj} and E_{hj} represent the minimum and maximum transition energy, respectively. Detailed description of all the parameters can be found in [12].

The measurement of the DLCH film CH30 carried out up to 30 eV was at first fitted independently. The data processing, data measured
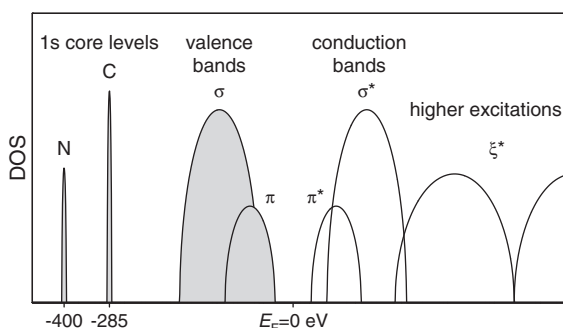

Fig. 1. Schematic diagram of the complete electronic structure of a-C:H:N. Shaded areas depict occupied electronic states. Symbol E_F denotes the Fermi energy.

Table 2
Summary of model parameters describing dielectric response of interband transitions in the DLCH (film CH30) and a-C:H:N (films CH16 and CH17) films. Dispersion model parameters are given in the first part of the table whereas the second part shows parameters related to film inhomogeneity and anisotropy.

Parameter/film	CH30	CH16	CH17
Q_π (eV$^{3/2}$)	9.88	10.94	8.68
$E_{g\pi}$ (eV)	0.752	0.509	0.440
$E_{h\pi}$ (eV)	9.03	8.70	8.70
$C_{0\pi}$	0.966	1.000	1.000
$E_{0\pi}$ (eV)	6.44	12.49	8.23
$B_{0\pi}$ (eV)	1.29	2.80	1.58
$Q_\sigma \equiv Q_\xi$ (eV$^{3/2}$)	68.62	66.82	64.28
$E_{g\sigma}$ (eV)	4.737	5.012	5.068
$E_{h\sigma}$ (eV)	28.1	28.1	28.1
$C_{0\sigma}$	0.694	0.694	0.694
$E_{0\sigma}$ (eV)	11.97	11.97	11.97
$B_{0\sigma}$ (eV)	3.26	3.26	3.26
$E_{g\xi}$ (eV)	12.14	12.14	12.14
$E_{h\xi}$ (eV)	39.3	39.3	39.3
p_π	1.158	1.438	1.070
p_σ	0.930	0.854	0.851
a	0.989	0.996	0.978

by all the instruments and their agreement with the fit in entire spectral range are discussed by Franta [13]. Afterwards, all the samples were fitted simultaneously. The ellipsometric and reflectance data in NIR–VUV compared with the fit are shown in Figs. 2 and 3. Because of the shorter measurement range of CH16 and CH17 all the parameters related to σ and $\xi*$ bands, except $E_{g\sigma}$ and Q_σ, were fixed at the values found for CH30. The parameter Q_ξ was set equal to Q_σ for all the films. Therefore, the total number of dispersion parameters in Table 2 was $6+6+2 = 14$.

The final values of the σ band gap $E_{g\sigma}$ of the individual films differed only slightly. The low energy $\sigma\rightarrow\sigma*$ transitions overlapped with $\pi\rightarrow\pi*$ transitions (see Fig. 4) and, therefore, this value cannot be determined directly from shape of dielectric function. The values of $E_{g\sigma}$ follows from the assumption of parabolic bands, i.e. square root-like shape of DOS in vicinity of band edges. Still, the values of $E_{g\sigma}$ were in the range 4.7–5.1 eV, i.e. in agreement with the band gap of crystalline diamond, 5.45–5.48 eV [21,22].

The changes of the parameters Q_σ and Q_π shown in Table 2 reflected changes of the density of σ and π electrons, i.e. changes of the bonding configuration in the films. The density of σ electrons corresponded to the density of strong bonds increasing the mechanical hardness. The parameter Q_σ decreased from the maximum value in DLCH film, CH30, to lower values in a-C:H:N. The hardness of the film CH16 was 18.5 GPa, i.e. slightly decreased in comparison with 21.7 GPa of CH30, whereas CH17 was quite soft polymeric film with the hardness of 6.7 GPa (Table 1). Therefore, the decrease of Q_σ between CH16 and CH17 was surprisingly small. The parameter Q_σ was probably not determined well in case of CH16 and CH17 because the measurement range was restricted to 10 eV and did not cover the full range of $\sigma\rightarrow\sigma*$ transitions whose maximum energy was 28.1 eV.

In case of CH16 and CH17 the higher band gap $E_{g\sigma}$ could suggest that the σ bands are narrower and the density of σ electrons is, therefore, overestimated.

The parameters describing the $\pi\rightarrow\pi*$ were all fitted independently because the maximum energy of transitions was expected below 10 eV. The $\pi\rightarrow\pi*$ band gap decreased from 0.752 eV for DLCH to 0.51–0.44 eV for a-C:H:N. For all three samples the shape of the π and $\pi*$ bands are asymmetrical and their shape close to the band gap is evidently far from square root-like form and it is more Gaussian-like (see Fig. 4). It is interesting that density of π electrons was higher in CH16 and lower in CH17 compared to CH30 (see parameter Q_π in Table 2). This is an illustration that the concentration of π electrons is not correlated with hardness of the material.
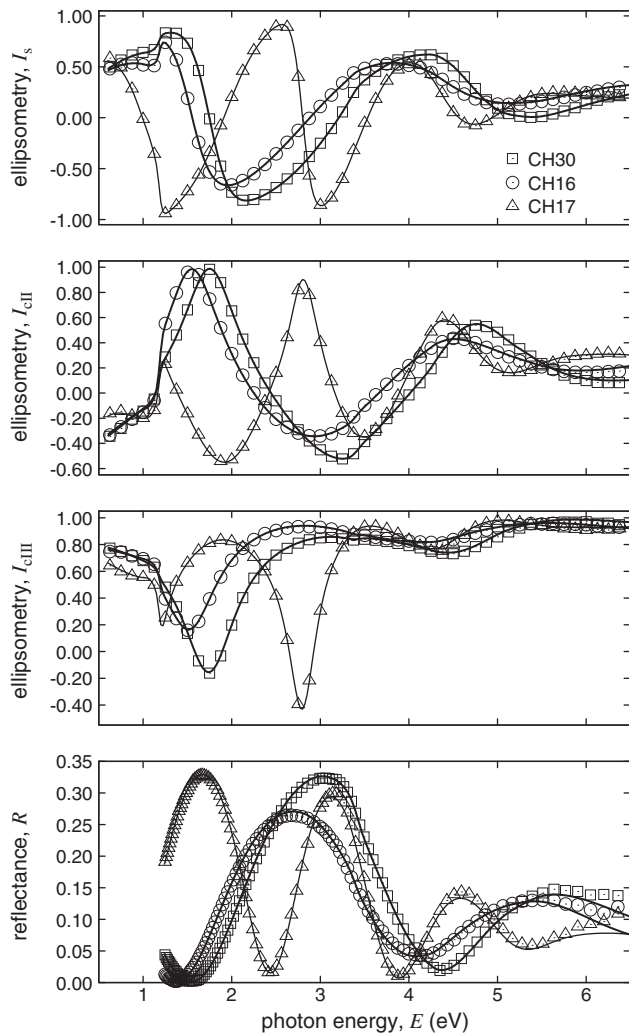
Fig. 2. Spectral dependencies of the associated ellipsometric parameters I_s, $I_{c,II}$, $I_{c,III}$ and reflectance R of samples CH30, CH16 and CH17 measured with table-top instruments: the lines and symbols denote theoretical and experimental data, respectively. The ellipsometric data correspond to the incidence angle of 65°.

3.2. Effect of film inhomogeneity, anisotropy and transition layer on NIR–XUV analysis

The film inhomogeneity brings another two parameters to the model, p_π and p_σ. They represent squared ratio of densities at the top, Q_j^{top}, and bottom, Q_j^{bot}, interface of the films as

$$p_j = \frac{\left(Q_j^{top}\right)^2}{\left(Q_j^{bot}\right)^2}. \tag{3}$$

The parameter Q_j, given in Table 2, is the mean squared density

$$Q_j^2 = \frac{\left(Q_j^{top}\right)^2 + \left(Q_j^{bot}\right)^2}{2}. \tag{4}$$

Real and imaginary parts of the dielectric function of a-C:H(:N) films at the top and bottom interfaces are compared in Fig. 5. The ratio p_π/p_σ higher than one means that the films contain more π electrons, i.e. more sp² bonded atoms, in their top regions. It can be probably explained by longer exposure of the bottom region to ion bombardment during film growth. Another possible explanation is photosensitivity of the material
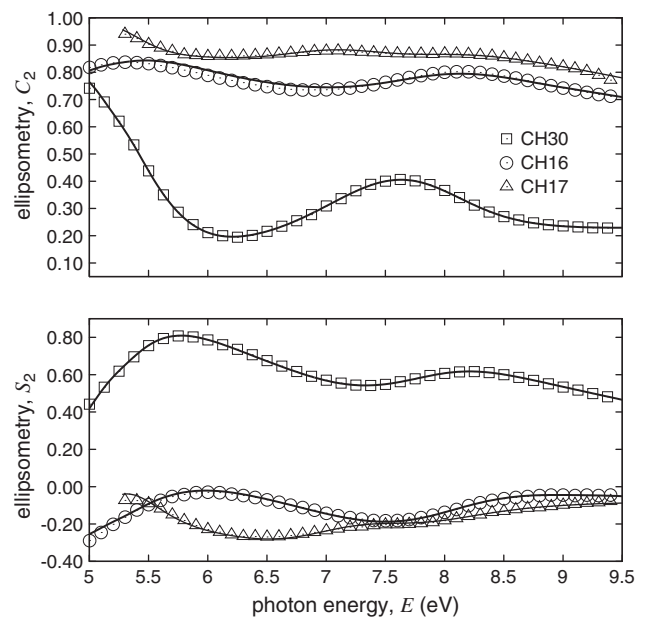

Fig. 3. Spectral dependencies of the second harmonic components C_2 and S_2 measured with BESSY II synchrotron ellipsometer at 67.5° in VUV spectral range for samples CH30, CH16 and CH17: the lines and symbols denote theoretical and experimental data, respectively.

to VUV light that has relatively small penetration depth. The synchrotron measurement was carried out after the table-top measurement and VUV light could modify the material. The CH16 table-top and synchrotron ellipsometric measurements were less compatible than in case of other two films. This caused worse agreement between
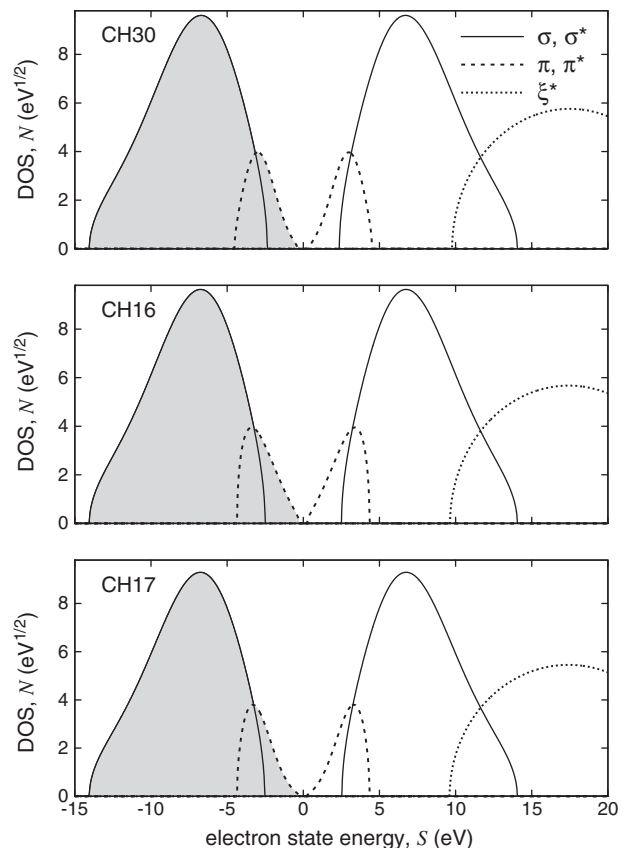

Fig. 4. DOS of electronic states of films CH30, CH16 and CH17 calculated from the best fit parameters. The DOS normalization corresponds to formula (2).
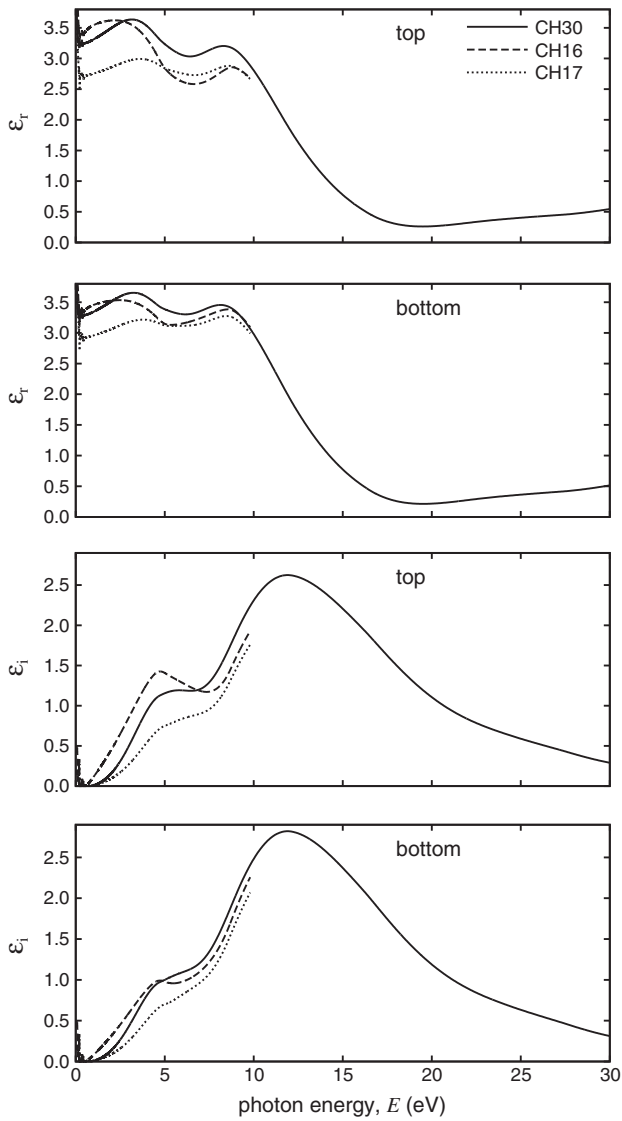
Fig. 5. Real and imaginary parts of the dielectric function of the DLCH film, CH30, and a-C:H:N films, CH16 and CH17, at their top and bottom interfaces.

the synchrotron data and the fit (Fig. 3). Therefore, the combination of both above effects probably took place in CH16. This film exhibited the highest inhomogeneity of π electrons, $p_\pi = 1.4$.

A weak stress-induced anisotropy of the films was introduced in the model similarly as in [12]. The anisotropy is parametrized by a single parameter a determining the ordinary, $\hat{\varepsilon}_o$, and extraordinary, $\hat{\varepsilon}_e$, dielectric functions:

$$\hat{\varepsilon}_o = a(\hat{\varepsilon}-1) + 1 \qquad \hat{\varepsilon}_e = \frac{1}{a^2}(\hat{\varepsilon}-1) + 1 \qquad (5)$$

where $\hat{\varepsilon}$ is the mean dielectric function.

The dielectric function of transition layers was modeled by parametrized JDOS model described in [19]. It resembled amorphous silicon or SiC material in the NIR–XUV region. Consistent understanding of transition layer band structure and inhomogeneity would require a specialized study using a set of samples with very thin a-C:H(:N) films. Here studied samples with the films having thickness 100–200 nm provide mostly information about dielectric response of a-C:H(:N) films and the influence of the transition layer on the measured quantities is hidden by the complexity of effects related to relatively thick films.

3.3. Analysis of optical measurement in IR region

A correct analysis of film absorption peaks in the measured transmittance of a thin film on absorbing substrate is not as simple as usually performed. Many authors use the Lambert–Beer law describing an attenuation of light intensity in homogeneous absorbing material. Since the substrate is absorbing the measured transmittance T is, in this approach, divided by the transmittance of substrate T_{sub} in order to "remove" the substrate absorption peaks:

$$T_{rel} = T / T_{sub}. \qquad (6)$$

This relative transmittance is then used to calculate the film absorbance A_f which is assumed proportional to the film absorption coefficient, i.e. the Lambert–Beer law is applied to the system with interfaces. Since the reflections at interfaces are usually non-negligible this approach has several weaknesses. The absorption peaks in the substrate, supposedly removed, can still appear in the analyzed film absorbance. Moreover, the analyzed film absorbance is influenced by the dispersion of the real part of refractive index. Therefore, the Lambert–Beer law based approximation is applicable only to weak absorption peaks or weak reflections at interfaces. Furthermore, the significant dispersion of real part of refractive index in the vicinity of strong absorption peaks causes peak asymmetry and shift of their positions.
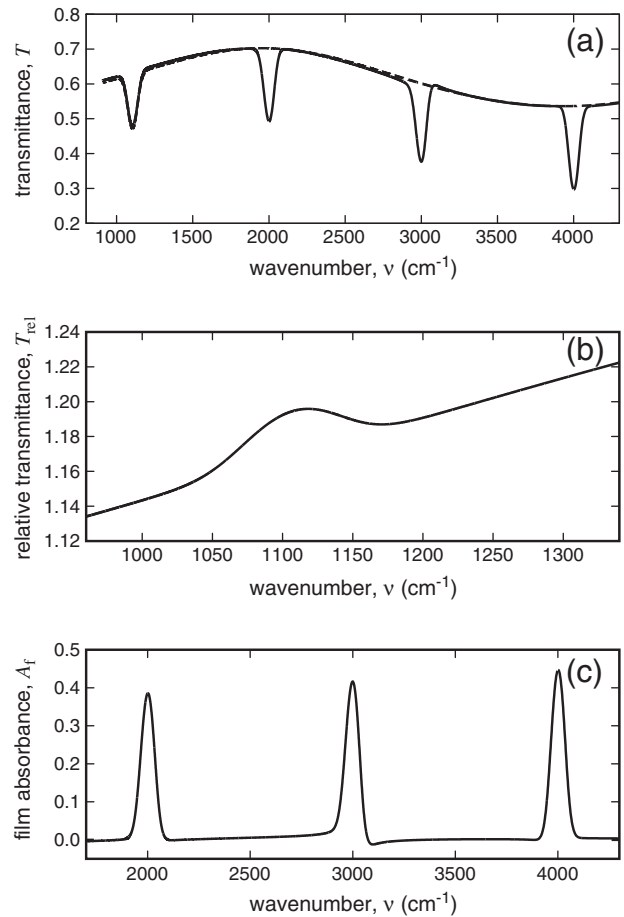

Fig. 6. Illustration of artifacts caused by naive evaluation of IR transmittance data: (a) simulated transmittance of a simple film-substrate system and "background" transmittance; (b) residuum of supposedly removed substrate absorption peak in the relative transmittance; (c) influence of peak position with respect to the interference minima and maxima on its apparent height and shape.

The weaknesses of the Lambert–Beer law approximation are demonstrated in Fig. 6 for a simplified system of a thin film exhibiting three identical Gaussian absorption peaks at 2000, 3000 and 4000 cm^{-1} on a substrate with one absorption peak at 1100 cm^{-1}. The mean refractive indices of the model film with the thickness of 680 nm and the substrate, 380 µm thick, correspond approximately to DLCH and silicon, respectively. The calculated transmittance T of this system is in Fig. 6a. Note that its overall shape is given by interference in the film (see dashed line, i.e. "background" transmittance T_{bg}). A "parasitic" peak obtained in relative transmittance T_{rel} at the position of substrate absorption is shown in Fig. 6b. Fig. 6c shows comparison of three peaks at different positions with respect to the interference maxima and minima after "background" interference was subtracted in film absorbance

$$A_f = 1 - T - R - A_s \approx \frac{T_{bg}}{T_{sub}} - T_{rel}, \tag{7}$$

where A_s is substrate absorbance. Although these peaks were identical in extinction coefficient they appear with different intensity. The effect of peak asymmetry can be seen, especially for a peak in sloping part of transmission, also from Fig. 6c.

Because of the above described effects measured IR transmittances of studied samples were fitted together with other optical data using a Kramers–Kronig consistent model. Within this model the joint density of states $J(E)$ corresponding to phonon absorption was described by a set of Gaussian peaks [19]:

$$J(E) = \sum_i \frac{A_i}{\sqrt{2\pi}B_i}\left\{\exp\left[-\frac{(E-E_i)^2}{2B_i^2}\right] - \exp\left[-\frac{(E+E_i)^2}{2B_i^2}\right]\right\}, \tag{8}$$

where A_i, B_i and E_i are the strength, broadening and position of i-th peak. Note that the positions of the Gaussian peaks are not the same as the positions of absorption peaks in imaginary part of dielectric function ε_i(E), extinction coefficient $k(E)$ and absorption coefficient $\alpha(E)$ because of following relations:

$$\varepsilon_i(E) = \frac{J(E)}{E^2} = 2n(E)k(E) = \frac{\hbar c}{E}\alpha(E)n(E), \tag{9}$$

where E is the energy in Joules, $n(E)$ denotes refractive index, h and c are Planck constant and vacuum light velocity, respectively. The peak position mismatch increases with increasing ratio of peak width to peak position or with strong dispersion of refractive index in the vicinity of absorption peak. Therefore, the comparison of peak positions among different authors has to be carefully performed taking into account Eq. (9) and effects of the Lambert–Beer law approximation discussed above. Parameter B_i is related to the peak full-width at half-maximum (FWHM) as follows:

$$\text{FWHM} = 2\sqrt{2\ln 2}B_i \approx 2.35B_i. \tag{10}$$

Since peak widths are commonly given as FWHMs we will follow this convention below to ease comparison with other works.

All the samples were fitted simultaneously using the multi-sample method. The advantage of this method consisted in better stability of fitting, especially in case of many free parameters. The positions and widths of the Gaussian absorption peaks were chosen as common multi-sample parameters. The strengths of the Gaussian peaks were searched separately for each sample.

The measured IR transmittance is shown in Fig. 7 for all three samples. The noticeably different values for the sample CH17 are caused by its different thickness. It can be seen that the transmittance below 1200 cm^{-1} is dominated by absorption in the Si substrate. This region was not suitable for precise fitting of film peaks because the dielectric function of the substrate was determined from measurement of an
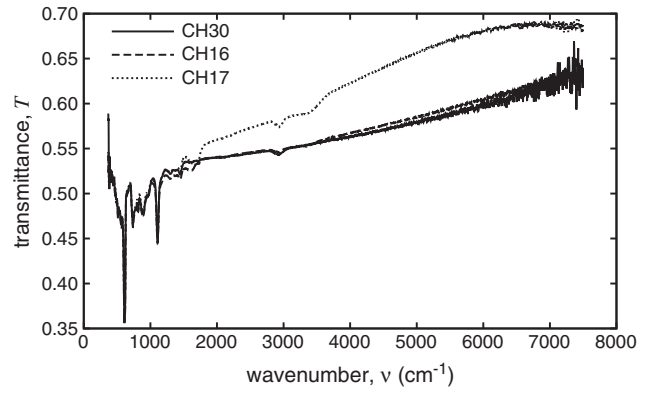

Fig. 7. Measured transmittances of the films CH30, CH16 and CH17 on Si substrates in the complete range of Bruker Vertex 80v spectrometer.

arbitrarily chosen Si piece and not by measuring of each Si substrate prior to the film deposition. Even though the substrate is cut from the same wafer as the reference the thickness can slightly differ leading to only partial compensation of substrate peaks. Additionally, different Si pieces can differ slightly in the amount of impurities that correspond to some absorption peaks. Therefore, a good agreement of the fit and the interpretation of fitted absorption peaks was sought only in the region above 1240 cm^{-1}.

Note that since IR transmittance is not sensitive to where in the film the absorption takes place the phonon contribution to ε_i was assumed to be homogeneous even though p_π/p_σ differed from unity, indicating different composition at the top and bottom of the film. The inhomogeneity of ε_r in IR region is thus given only by inhomogeneity of contributions of interband transitions. Both parts of the dielectric function are shown in Fig. 8.
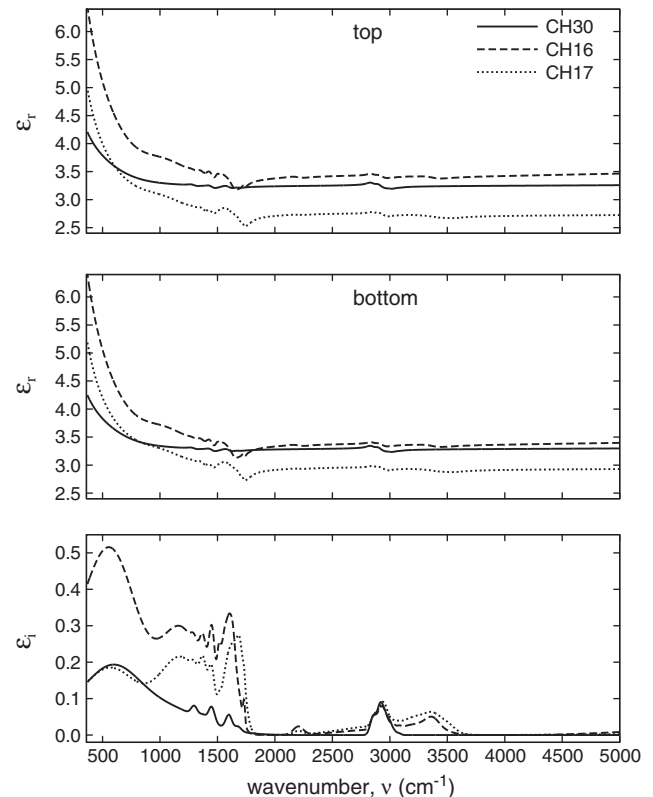

Fig. 8. Real and imaginary part of the dielectric function of all three films in IR region.

3.4. Chemical structure and lattice vibrations of the films

Information about chemical composition of the films was obtained using the combination of RBS and ERDA methods. It provided complete atomic composition of the films including the hydrogen content. Traces of argon (below 0.3%) were attributed to the incorporation of argon into the Si substrate during plasma pretreatment. The films were mainly composed of hydrogenated carbon as summarized in Table 1. The films CH16 and CH17, deposited from $CH_4/H_2/N_2$ mixture, contained 13 and 10% of nitrogen, respectively. All the films contained a small amount of oxygen. The base pressure in the reactor chamber was below 10^{-3} Pa and the leak/desorption rate was below 0.02 sccm. Therefore, oxygen had to be incorporated into the film structure after exposure to atmosphere. This can also explain the different amounts of oxygen in the films because vacuum conditions during the deposition were similar but post-deposition oxygen incorporation depended on the material chemical structure that was affected by differing deposition conditions. Namely, the oxygen content increased for nitrogen containing films and soft polymer-like film CH17.

The analysis of lattice vibrations provides more detail information about the chemical structure of the films. It starts in following text from the high frequency part of measured IR transmittance – region of group frequencies. Absorption peaks attributed to C—H stretching of hydrocarbon groups are generally found in the region 2850–3100 cm^{-1}. The peaks below 3000 cm^{-1} are mostly related to vibration modes present in saturated hydrocarbons, i.e. sp^3C—H_x $(x=1,2,3)$. These group frequencies are similar for different compounds because of little coupling to the rest of molecular system and can be, therefore, predicted quite exactly. Stretching of sp^2C—H_x $(x=1,2)$ can be found above 3000 cm^{-1} [23].

The C—H stretching peaks strongly overlapped and formed a distinct absorption band (Figs. 7 and 9). The absorption above 3000 cm^{-1}, related to sp^2C, was a weak shoulder of the band (Fig. 9b, d). The positions of fitted peaks were fixed at following values: 2915 cm^{-1} assigned as C—H stretching in sp^3C—H, 2855, 2925, 2870 and 2960 cm^{-1} assigned as symmetric and antisymmetric stretching in sp^3C—H_2 and sp^3C—H_3, respectively [23,24], 3000 and 3080 cm^{-1} associated with symmetric and asymmetric stretch of olefinic sp^2C—H_2, 3030 and 3050 cm^{-1} associated with stretch of olefinic sp^2C—H and aromatic sp^2C—H, respectively [23]. The widths of C—H stretching peaks were kept as an identical fitting parameter for sp^3C—H_x and sp^2C—H_x separately. The previously published FWHMs were in the range 70–90 cm^{-1} [24]. Our best fit corresponded to 60 and 44 cm^{-1} of peak FWHM, respectively. The agreement between the measured and theoretical transmittances is shown for the sample CH30 in Fig. 9b. The imaginary part of dielectric function, ε_i, of all three films and contribution of the C—H stretching to ε_i are depicted in Fig. 9c and d. The summary of fitting results and peak assignment are in Table 3.

The films deposited with nitrogen addition were characterized by wide absorption peaks in the range 2950–3500 cm^{-1}. Their parameters, i.e. position, width and strength, were set free, however, the position and width were kept identical for both CH16 and CH17. The resulting peak parameters are summarized in Table 3 and their contribution to the imaginary part of dielectric function is shown in Fig. 10d, e. Since the peaks were wide their positions in JDOS and $\varepsilon_i(E)$ differed. The FWHM of the JDOS peak at 3372 cm^{-1} was 136 cm^{-1} and its position in ε_i was shifted to lower frequencies by 2 cm^{-1}. However, the widest peak at 2949 cm^{-1} was shifted by as much as 64 cm^{-1}.

The peak strengths were higher for the film CH17 that contained more oxygen with the exception of the peak at 3372 cm^{-1}. This relatively narrow peak (compare FWHM of 136 cm^{-1} to 167–713 cm^{-1} in Table 3) could be perhaps assigned to NH stretching because it was slightly stronger in the film CH16 containing more nitrogen. Rodil [25] assumed that the peaks related to the NH or OH bonds formed during the deposition are narrower and this argument also justifies the assignment of the NH bonds. The other peaks were attributed to OH groups. The incorporation of oxygen containing groups into a-C:H and
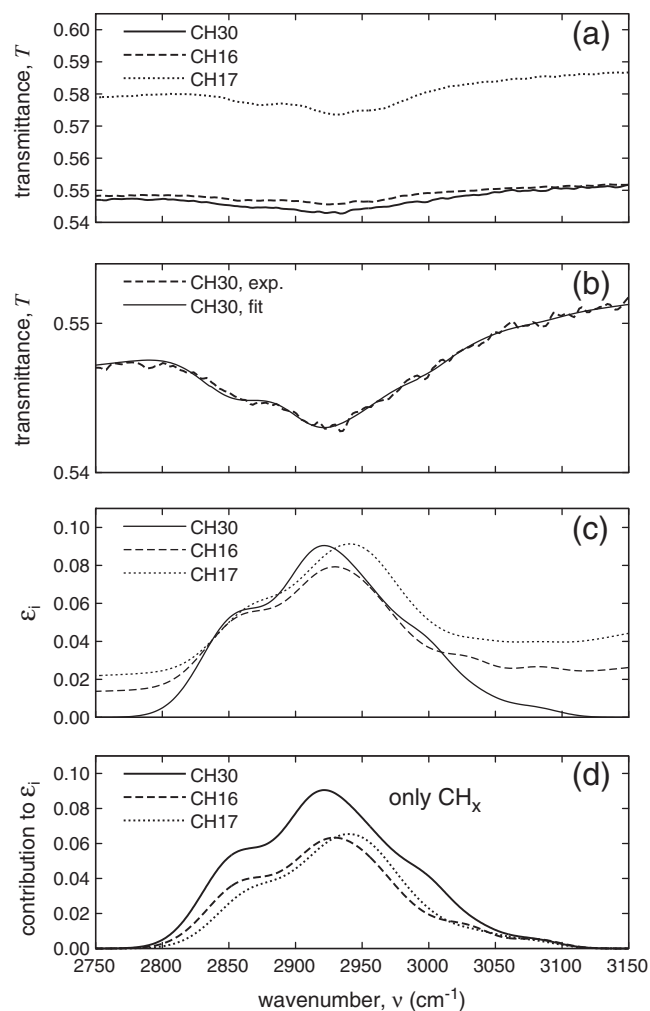

Fig. 9. Infrared spectra in range 2750–3150 cm^{-1}: (a) measured transmittances of all three samples; (b) comparison of the measurement and fit for the sample CH30; (c) imaginary part of dielectric function ε_i of all three films (d) contribution of the C—H stretching.

especially a-C:H:N films have been already observed by other authors too and its assumed to take place in case of soft, rough or porous films [26]. The optical measurements confirmed that the films do not exhibit any roughness but the film with the most of OH groups, CH17, was indeed soft, polymer-like material in which adsorption of water can easily take place by formation of hydrogen bonds.

The absorption peak observed at 2100 cm^{-1} in the transmittances of all samples was assigned to Si–H stretching (Fig. 7b). It was attributed to the transition layer created by plasma modification of Si substrate. Its position, width and strength were set identical for all the samples. In spite of this restriction the agreement between the measurement and the fit was satisfactory (shown for an arbitrary chosen sample CH16 in Fig. 10b). It confirmed that this peak can be really attributed to the transition layer that was similar for all three samples. The peak at 2205 cm^{-1} was observed only in a-C:H:N and, therefore, the assignment to nitrile —C≡N, isonitrile —N≡C and/or carbodi-imide —N=C=N— [23,25,27] is clearly justified.

Additional film absorption peaks were observed in low frequency region (Figs. 11 and 12). According to the above discussion of the Si substrate effect the detailed analysis is restricted to the peaks from 1240 cm^{-1}. Note that two broad peaks positioned at 720 and 1212 cm^{-1} were necessary for good agreement with measured data (Fig. 12b). Their contribution to ε_i is shown in Fig. 12d.

Table 3
Parameters of Gaussian peaks describing film dielectric response in IR range, i.e. peak positions, FWHMs and strengths, found by multi-sample fitting the optical data of CH30, CH16 and CH17 films on Si substrate. The position and FWHM of the peaks were kept identical for all three samples whereas the strengths were independent parameters.

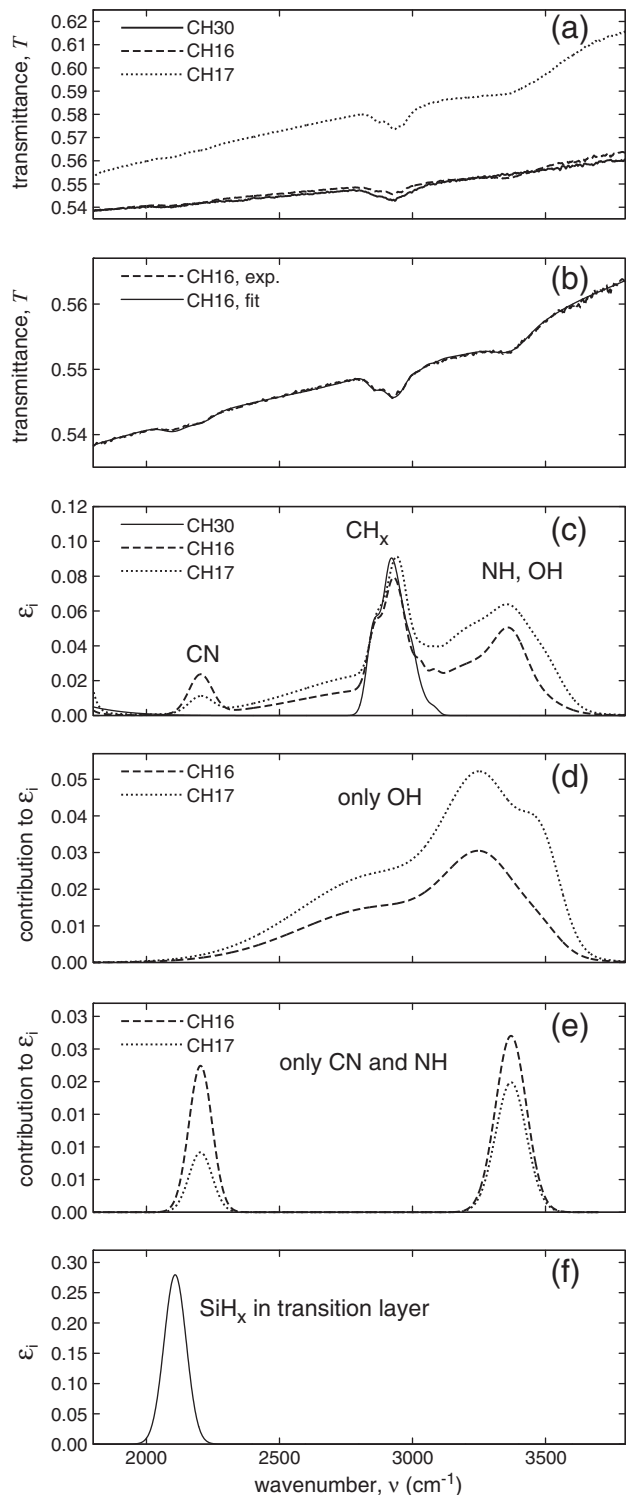| Position (cm^{-1})	FWHM (cm^{-1})	Strength			Vibration mode
		CH30	CH16	CH17	
CH stretching					
3080	44	38	44	31	sp^{2}C—H$_2$ olef. sym.
3050	44	26	0	29	sp^{2}C—H arom.
3030	44	81	89	53	sp^{2}C—H olef.
3000	44	197	52	69	sp^{2}C—H$_2$ olef. asym.
2960	60	512	363	452	sp^{3}C—H$_3$ asym.
2925	60	19	240	324	sp^{3}C—H$_2$ asym.
2915	60	764	277	122	sp^{3}C—H
2870	60	0	117	243	sp^{3}C—H$_3$ sym.
2855	60	494	246	68	sp^{3}C—H$_2$ sym.
OH/NH/CN					
3493	167	0	154	927	O—H
3372	136	0	848	625	N—H
3281	320	0	1625	2836	O—H
2949	713	0	1856	2971	O—H
2205	102	0	227	93	C≡N/N≡C/−N=C=N−
CC/CO/OH					
1732	19	0	65	31	C=O
1695	106	0	57	1328	C=O/N-induced sp^{2}C
1680	64	45	42	181	sp^{2}C
1652	111	0	773	0	N-induced sp^{2}C/O—H
1638	45	0	180	158	N-induced sp^{2}C/O—H
1600	64	128	655	542	sp^{2}C
1553	57	0	456	218	N-induced sp^{2}C
1513	38	0	217	69	N-induced sp^{2}C
1300	64	56	68	52	sp^{2}C
1248	441	0	3766	2573	N-induced sp^{2}C
CH deformation					
1460	64	0	177	0	sp^{3}C—H$_3$ asym. bend.
1450	64	119	346	287	sp^{3}C—H$_2$ scissoring
1375	64	29	233	199	sp^{3}C—H$_3$ sym. bend.
Unidentified peaks below 1240 cm^{-1}					
1212	737	1402	0	346	
720	508	671	2188	747	

Fig. 10. Infrared spectra in range 1800–3800 cm^{-1}: (a) measured transmittances of all three samples; (b) comparison of the measurement and fit for the sample CH16; (c) imaginary part of dielectric function ε_i (d) contribution of OH; (e) contribution CN and NH; (f) ε_i corresponding to the Si-H stretching peak in the transition layer.

The measured transmittances in the range 1200–1850 cm^{-1} are shown for all three samples in Fig. 11a. Three absorption bands at about 1300, 1375 and 1450 cm^{-1} were well separated in the region of C—H deformations, i.e. below 1500 cm^{-1}. They were fitted by four peaks with their positions fixed at 1300, 1375, 1450 and 1460 cm^{-1}. The FWHMs of the peaks were assumed to be identical and the best fit corresponded to 64 cm^{-1}. The contribution of these peaks to the imaginary part of dielectric function is shown in Fig. 11d. The selection and assignment of the peak positions are discussed below on the basis of previously published papers.

Antisymmetric bending of methyl, sp^{3}C—H$_3$, was previously observed from 1460 cm^{-1} [23,28] to 1490 cm^{-1} [29]. The scissoring of methylene, sp^{3}C—H$_2$, was positioned at 1450 cm^{-1} [23,28,29] and the symmetric bending of sp^{3}C—H$_3$ at 1375 cm^{-1} [23,28]. As for the C—H stretching, only a little coupling of these deformations to the rest of material is expected. Wagging and twisting modes of methylene at around 1300 cm^{-1} are usually weak in infrared spectra and their positions are coupled to chemical environment [23]. The relatively strong peak at 1300 cm^{-1} was, therefore, assigned rather to the collective vibration of carbon skeleton following Theye [30,31]. Deformations of sp^{2}C—H$_x$ either strongly overlapped with sp^{3}C—H$_2$ [29] or, if positioned at about 1400 cm^{-1} [28], they were too weak.

In a-C:H films, a well-defined peak found in the region 1580–1640 cm^{-1} have been already unambiguously attributed to the stretching modes of sp^{2}C double bonds in aromatic or olefinic configurations [30,32]. Its position shifted to higher frequencies for chain structures of olefins observed in polymeric films whereas frequency below 1600 cm^{-1} was assigned to ring structure of sp^2 clusters in hard films
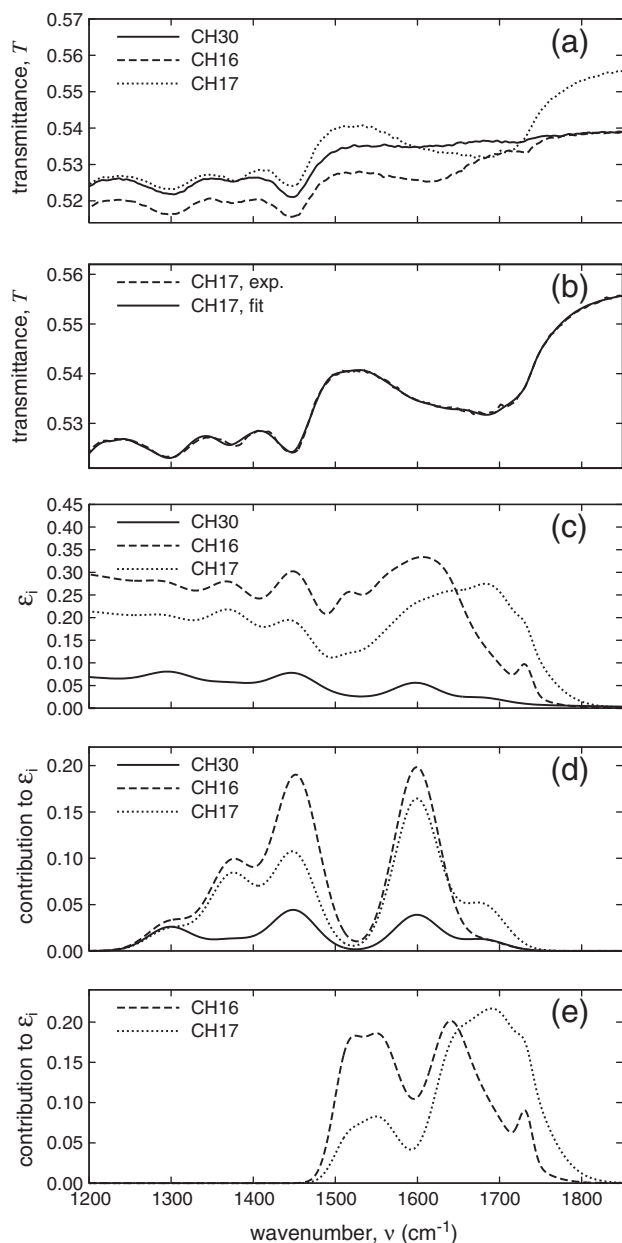
Fig. 11. Infrared spectra in range 1200–1850 cm^{-1}: (a) measured transmittances of all three samples; (b) comparison of the measurement and fit for the sample CH17; (c) imaginary part of dielectric function ε_i; (d) contributions related to the peaks found in all three films; (e) contributions of the peaks found solely in a-C:H:N, i.e. CH16 and CH17.

Fig. 12. Infrared spectra in range 360–1600 cm^{-1}: (a) measured transmittances of all three samples; (b) comparison of the measurement and fit for the sample CH16; (c) imaginary part of dielectric function ε_i of all three films (d) contribution of the broad peaks.

[30,31]. In this work, two peaks with fixed positions at 1600 and 1680 cm^{-1} were included in JDOS of all the films. The corresponding absorption peaks in transmittance of DLCH were very weak, especially in case of the peak at 1680 cm^{-1}.

The above discussed peaks centered in the region 1375–1600 cm^{-1} were much stronger for a-C:H:N films as shown in Fig. 11d. Moreover, the a-C:H:N films required addition of a strong wide peak at 1248 cm^{-1} (FWHM 442 cm^{-1}), two weaker sharper peaks at 1513 and 1553 cm^{-1} and several peaks in the region above 1600 cm^{-1} (Table 3). The contribution of these peaks is depicted in Fig. 11e. The peaks at 1513 and 1553 cm^{-1} formed one broad flat or asymmetric band. The peaks at 1638, 1652 and 1695 cm^{-1} composed a broad band centered at 1632 and 1683 cm^{-1} for CH16 and CH17, respectively. The peak at 1732 cm^{-1} was well separated from this band in case of CH16.

The absorption bands in the region 1000–1700 cm^{-1} for a-C:H and especially a-C:H:N films were matter of a long term discussion and very
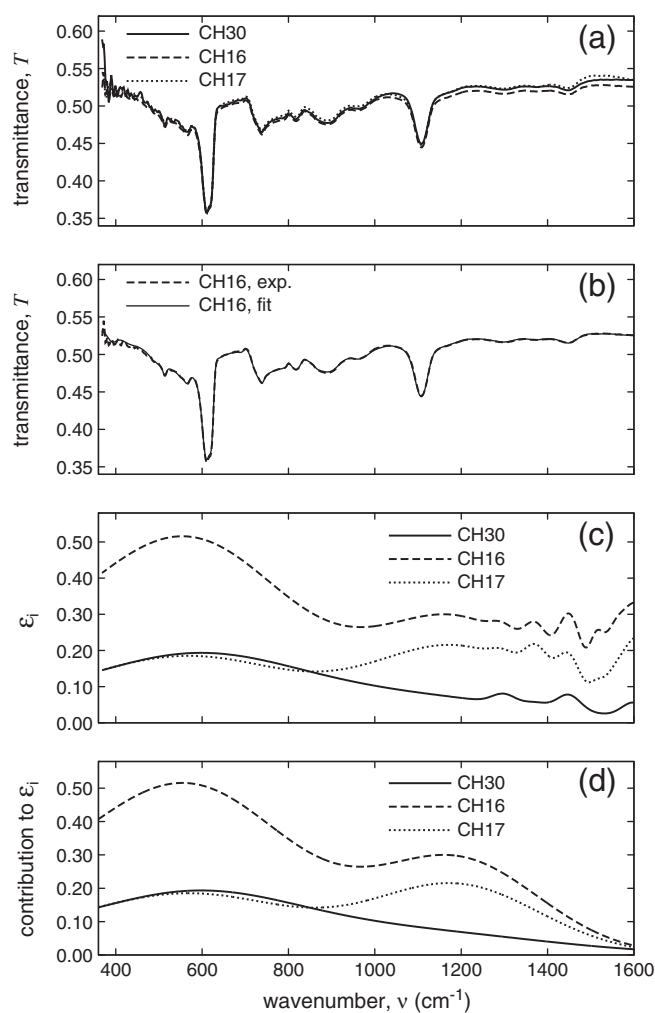
different assignments can be found in previously published papers. Theye [30] shifted deformation modes of C−H bonds to lower frequencies by replacing H by D and observed two broad bands centered at 1300–1350 and 1580–1630 cm^{-1} assigned to carbon skeletal vibrations. A weak absorption at the positions 1300, 1600 and 1680 cm^{-1} was observed also in here studied DLCH film CH30 (discussed above). The approach of Theye was adopted by Ferrari [33] for a-C(:H):N films. They assumed that major absorption band observed in the 1000–1650 cm^{-1} region was due to sp^{2}C vibrations and not due to specific CH, CN, NH and NN vibrations. The increase of absorption in case of increased nitrogen content was explained by polarization of sp^{2}C phase induced by the terminal N atoms. The shape of this band changed with the type of the films. Accordingly, increased strength and addition of some peaks in case of the films CH16 and CH17 was attributed to sp^{2}C phase vibrations. Part of this absorption at higher frequencies can be, however, also assigned to the bending mode of water observed in a-C:N(:H) films at about 1610–1640 cm^{-1} [26] and stretching of carbonyl group whose typical frequency is around 1720 cm^{-1}[23]. The carbonyl frequency is quite variable depending on the chemical surrounding. Indeed, the absorption at frequencies above 1650 cm^{-1} was higher in the film CH17 that contained more oxygen than CH16 and had more polymeric character.

It is worth noting that the assignment of increased absorption in the range 1200–1650 cm^{-1} to increased optical activity of sp^{2}C phase induced by the presence of nitrogen corresponded to the results from

NIR–VUV region because the density of π electrons, obtained from NIR–VUV measurement, as well as the infrared absorption in 1200–1650 cm^{-1} was higher in CH16 than in CH17.

4. Conclusion

The combination of measurements carried out with two spectro-photometers, synchrotron and table-top ellipsometers provided optical data in a wide spectral range (IR–XUV) that were simultaneously fitted by the Kramers–Kronig consistent model taking into account electronic interband transitions and lattice vibrations. This unique approach provided parameters describing DOS of valence and conduction bands, i.e. bonding structure, and revealed complicated infrared absorption induced by nitrogen incorporation. Three broad peaks in range 2950–3500 cm^{-1} corresponded to increased incorporation of oxygen containing groups especially in polymer-like a-C:H:N films. The increased absorption in the range 1000–1700 cm^{-1} for a-C:H:N mainly corresponded to polarization of sp^{2}C phase induced by nitrogen and its shape changed with the film hardness. The density of σ electrons decreased with decreasing hardness for both the a-C:H:N films as compared to the hydrogenated diamond like carbon (DLCH) film with hydrogen content of 34% and indentation hardness of 21.7 GPa. The density of π electrons increased for the hard a-C:H:N film (13% of nitrogen, hardness 18.5 GPa) and decreased for the soft a-C:H:N film (10% of nitrogen, hardness 6.7 GPa). Therefore, the soft film prepared at lower dc self-bias had a considerably lower electron density. The results were in agreement with the expected correlations between the material bonding structure and hardness, confirming the correctness of the applied model. However, the a-C:H:N films were not measured in the spectral range covering all $\sigma \rightarrow \sigma$ transitions and, therefore, parameters of σ bands might not be reliably determined. Parameters of $\pi \rightarrow \pi$ transitions were more reliable because the maximum energy of transitions was about 10 eV. Considering these issues the described approach could utilize table-top ellipsometers working in VUV range (up to 10 eV) instead of synchrotron ellipsometry and, therefore, be applied to a wider group of a-C:H:N films.

Acknowledgements

References

[1] C. Casiraghi, A.C. Ferrari, J. Robertson, Phys. Rev. B 72 (2005) 1.
[2] C. Donnet, A. Erdemir, Tribology of Diamond-like Carbon films: Fundamentals and Applications, Springer, 2007.
[3] A.C. Ferrari, Surf. Coat. Technol. 180–181 (2004) 190.
[4] A.C. Ferrari, J. Robertson, M.G. Beghi, C.E. Bottani, R. Ferulano, R. Pastorelli, Appl. Phys. Lett. 75 (1999) 1893.
[5] A.C. Ferrari, A. Libassi, B.K. Tanner, V. Stolojan, J. Yuan, L.M. Brown, S.E. Rodil, B. Kleinsorge, J. Robertson, Phys. Rev. B 62 (2000) 11089.
[6] N.A. Morrison, S.E. Rodil, A.C. Ferrari, J. Robertson, W.I. Milne, Thin Solid Films 337 (1999) 71.
[7] M.-L. Thèye, V. Paret, Carbon 40 (2002) 1153.
[8] M. Nöthe, U. Breuer, F. Koch, H.J. Penkalla, W.P. Rehbach, H. Bolt, Appl. Surf. Sci. 179 (2001) 122.
[9] R. Rabbani, R. Escobar Galindo, W.M. Arnoldbik, S. van der Zwaag, A. van Veen, H. Schut, Diamond Relat. Mater. 13 (2004) 1645.
[10] Y. Hayashi, K.M. Krishna, H. Ebisu, T. Soga, M. Umenob, T. Jimbo, Diamond Relat. Mater. 10 (2001) 1002.
[11] M.K. Arora, A.H. Lettington, D.R. Waterman, Diamond Relat. Mater. 8 (1999) 623.
[12] D. Franta, D. Nečas, L. Zajíčková, V. Buršíková, C. Cobet, Diamond Relat. Mater. 19 (2010) 114.
[13] D. Franta, D. Nečas, L. Zajíčková, V. Buršíková, C. Cobet, Thin Solid Films 519 (2011) 2694.
[14] L. Zajíčková, D.P. Subedi, V. Buršíková, K. Veltruská, Acta Phys. Slovaca 53 (2003) 489.
[15] M.A. Lieberman, A.J. Lichtenberg, Principles of Plasma Discharges and Materials Processing, John Wiley & Sons, New York, 1994.
[16] J. Saarilahti, E. Rauhala, Nucl. Instrum. Methods B 64 (1992) 734.
[17] M. Mayer, SIMNRA user's guide, Technical report ipp 9/113, Max-Planck-Institut fuer Plasmaphysick, Garching, Germany, 1997.
[18] http://www-nds.iaea.org/ibandl.
[19] D. Franta, D. Nečas, L. Zajíčková, Opt. Express 15 (2007) 16230.
[20] D. Franta, D. Nečas, L. Zajíčková, V. Buršíková, Diamond Relat. Mater. 18 (2009) 413.
[21] M. Nesládek, K. Meykens, L.M. Stals, M. Vaněček, J. Rosa, Phys. Rev. B 54 (1996) 5552.
[22] C.E. Nebel, Semicond. Sci. Technol. 18 (2003) S1.
[23] D. Mayo, F.A. Miller, R.W. Hannah, Course Notes on the Interpretation of Infrared and Raman Spectra, Wiley-Interscience, New York, 2004.
[24] B. Dischler, A. Bubenzer, P. Koidl, Solid State Commun. 48 (1983) 105.
[25] S.E. Rodil, A.C. Ferrari, J. Robertson, S. Muhl, Thin Solid Films 420–421 (2002) 122.
[26] S.E. Rodil, Diamond Relat. Mater. 14 (2005) 1262.
[27] R. Ohta, N. Saito, S. Okayaki, Y. Inoue, H. Sugimura, O. Takai, Thin Solid Films 457 (2004) 128.
[28] T. Heitz, B. Drévillon, C. Godet, J.E. Bourée, Phys. Rev. B 58 (1998) 13957.
[29] B. Dischler, Amorphous hydrogenated carbon films, in: P. Koidl, P. Oelhafen (Eds.), Proceedings of the EMRS Symposium, Vol. 17 of Les Editions de Physique, Paris, 1987, p. 189.
[30] M.-L. Thèye, V. Paret, A. Sadki, Diamond Relat. Mater. 10 (2001) 182.
[31] J. Robertson, Mater. Sci. Eng., R 37 (2002) 129.
[32] M.-L. Thèye, V. Paret, A. Sadki, Condens. Matter News 7 (1998) 4.
[33] A.C. Ferrari, S.E. Rodil, J. Robertson, Phys. Rev. B 67 (2003) 155306.